Lithos 178 (2013) 197–210

Contents lists available at ScienceDirect

Lithos

journal homepage: www.elsevier.com/locate/lithos

Pressure–temperature estimates of the lizardite/antigorite transition in high pressure serpentinites

Stéphane Schwartz [a,*], Stéphane Guillot [a], Bruno Reynard [b], Romain Lafay [a], Baptiste Debret [c], Christian Nicollet [c], Pierre Lanari [a], Anne Line Auzende [d]

[a] IsTerre, Université Grenoble 1, CNRS, F-38041 Grenoble, Cedex 9, France
[b] Laboratoire de Géologie, Ecole Normale Supérieure de Lyon, CNRS, France, Site Monod, 15 parvis René Descartes, Lyon, F-69342, France
[c] LMV, Université Blaise Pascal, CNRS, Clermont-Ferrand, France
[d] IMPMC, Université Pierre et Marie Curie - Sorbonne Universités, 4 place Jussieu, Tour 23, 75252 Paris Cedex 05, France

ARTICLE INFO

Article history:
Received 23 September 2012
Accepted 24 November 2012
Available online 5 December 2012

Keywords:
Serpentinite
Raman spectroscopy
Lizardite/antigorite transition
Western Alps

ABSTRACT

Serpentine minerals in natural samples are dominated by lizardite and antigorite. In spite of numerous laboratory experiments, the stability fields of these species remain poorly constrained. This paper presents petrological observations and the Raman spectroscopy and XRD analyses of natural serpentinites from the Alpine paleo-accretionary wedge. Serpentine varieties were identified from a range of metamorphic pressure and temperature conditions from sub-greenschist (P<4 kbar, T~200–300 °C) to eclogite facies conditions (P>20 kbar, T>460 °C) along a subduction geothermal gradient. We use the observed mineral assemblage in natural serpentinite along with the T_{max} estimated by Raman spectroscopy of the carbonaceous matter in associated metasediments to constrain the temperature of the lizardite to antigorite transition at high pressures. We show that below 300 °C, lizardite and locally chrysotile are the dominant species in the mesh texture. Between 320 and 390 °C, lizardite is progressively replaced by antigorite at the grain boundaries through dissolution–precipitation processes in the presence of SiO_2 enriched fluids and in the cores of the lizardite mesh. Above 390 °C, under high-grade blueschist to eclogite facies conditions, antigorite is the sole stable serpentine mineral until the onset of secondary olivine crystallization at 460 °C.

1. Introduction

Serpentine minerals are phyllosilicates that contain up to 13 wt.% water and form during the hydration of basic to ultrabasic rocks. Hydration commonly takes place in an ocean spreading context, thus documenting chemical exchanges between the oceans and solid Earth (Alt and Shanks, 2003). Serpentinites are also common in blueschist to eclogite facies terranes of oceanic or mantle wedge origin (Hattori and Guillot, 2007). Due to the large metamorphic stability field of serpentinites, it is generally difficult to evaluate the P–T conditions to which they were subjected (e.g., Evans, 2004), but the associated metamorphic rocks permit approximations of the conditions. It is therefore important to accurately and rapidly characterize these common serpentine minerals. Serpentine minerals, which have the simplified structure formulae $(Mg, Fe^{2+})_3\ Si_2O_5(OH)_4$, are made of superposed 1:1 alternating tetrahedral and octahedral sheets. The different spatial arrangements of these layers result in three main serpentine minerals, i.e., lizardite, chrysotile and antigorite. The sheets form flat layers in lizardite, cylinders in chrysotile and corrugated modulated structures in antigorite (Wicks and O'Hanley, 1988). Serpentinites in high-grade metamorphic terranes indicate that antigorite is the predominant species (Auzende et al., 2002, 2006; Debret et al., 2013; Evans and Tromsdorff, 1978; Groppo and Compagnoni, 2007; Guillot et al., 2009; Li et al., 2004; Mellini et al., 1987; Padron-Navarta et al., 2008; Scambelluri et al., 1995; Trommsdorff et al., 1998). Moreover, experimental studies confirm that antigorite is the stable serpentine mineral under high-pressure conditions (Bromiley and Pawley, 2003; Padron-Navarta et al., 2010; Reynard and Wunder, 2006; Ulmer and Trommsdorff, 1995; Wunder and Schreyer, 1997). Lizardite and chrysotile are the main varieties that are present in low-grade serpentinites from the oceanic lithosphere and from low-grade metamorphic ophiolites (Andréani et al., 2007; Evans, 2004). However, the transition from low-grade to high-grade metamorphic serpentine minerals is poorly constrained. Thermodynamic data predict that above 300 °C, the antigorite + brucite assemblage is more stable than lizardite, and chrysotile is absent (Evans, 2004). Moreover, the antigorite + brucite assemblage is often observed in natural samples, while the chrysotile + brucite assemblage is particularly abundant in retrogressed serpentinites (Baronnet and Belluso, 2002). Thus, further petrological investigations of natural serpentinite samples, where the P–T conditions are well-constrained, are required to refine the relative stability of each variety of serpentine over a wide range of metamorphic conditions. To definitively identify serpentine varieties, transmission electron microscopy (TEM)

* Corresponding author.
E-mail address: stephane.schwartz@ujf-grenoble.fr (S. Schwartz).

0024-4937/$ – see front matter © 2012 Elsevier B.V. All rights reserved.
http://dx.doi.org/10.1016/j.lithos.2012.11.023

is usually required (Auzende et al., 2002; Boudier et al., 2010; Mellini et al., 1985). Indeed, serpentine grains are in some cases only a few microns in size and can display various habitus, which makes optical identification inaccurate. Vibrational Raman spectroscopy is also a powerful method for processing large numbers of complex samples, and numerous studies have been devoted to its use in serpentine characterization (Auzende et al., 2004; Bard et al., 1997; Groppo et al., 2006; Kloprogge et al., 1999; Lewis et al., 1996; Rinaudo et al., 2003). In particular, the region of the OH stretching vibrational modes can be conveniently used to discriminate among the different varieties of serpentine (Auzende et al., 2004). The OH stretching modes in the high wavenumber range (approximately 3500 cm^{-1}) of the different serpentines are tentatively described in terms of the curvature of the layers, with potential applications for structural characterization by Raman spectroscopy. Raman spectroscopy permits the characterization of the phases at a micrometer scale of bulk samples or thin sections. To assess the reliability of Raman spectroscopy for identification purposes, we apply it to serpentines in a series of low to high pressure metamorphic serpentinite samples from the western Alps for which TEM characterization have been independently performed (Auzende et al., 2006). The serpentinites are also characterized by X-ray diffraction (XRD) in order to decipher the bulk serpentinite mineralogy.

2. Geological setting

Alpine evolution along the Eurasia-Africa boundary was initially dominated by plate divergence, which induced Mesozoic rifting and oceanic opening. Since Cretaceous time, the plate convergence has resulted in subduction and collision (Dumont et al., 2012; Rosenbaum and Lister, 2005). This study focuses on the Piedmont zone of the southwestern Alps (Fig. 1a and b), which is composed of the association of units that originated in the distal European margin and from the nearby oceanic domain (Lemoine et al., 1987) and that were juxtaposed during the subduction and collision in Late Cretaceous to Tertiary times (Tricart, 1984). The Piedmont zone includes different levels of the paleo-subduction zone, preserving the low thermal gradient (5–8 °C/km) associated with the subduction dynamics; moreover, it was partially overprinted by Alpine metamorphism conditions (Agard et al., 2002; Schwartz et al., 2001, 2007). At the top of the nappe pile, the Chenaillet massif corresponds to an obducted portion of the Tethyan oceanic lithosphere. This unit rests upon the Queyras Schistes lustrés (Fig. 1c), which represent a fossiliferous sedimentary accretionary wedge developed under blueschist facies conditions during the late Cretaceous–early Eocene subduction of the Tethyan Ocean (Schwartz et al., 2000, 2009; Tricart and Schwartz, 2006), as previously indicated by structural observations further to the north in the same Piedmont zone (Agard et al., 2001; Ganne et al., 2005). This domain derived from Mesozoic oceanic sediments that were primarily composed of marls, clays, and limestones (calcschists). These sediments were strongly deformed and metamorphosed during alpine subduction, and they outcrop today as foliated and polydeformed calcschists enclosing boudinaged meter- to kilometer-sized Jurassic ophiolites (Lagabrielle and Polino, 1988; Tricart and Lemoine, 1986). The P–T conditions increase toward the east, from low-temperature blueschist facies conditions (LT-blueschist) in western Queyras to the transitional conditions between high-temperature blueschist (HT-blueschist) and eclogite facies in eastern Queyras (Agard et al., 2001; Schwartz et al., 2009; Tricart and Schwartz, 2006). This blueschist domain is structurally above the Monviso eclogitic ophiolite. In this massif, the metasedimentary component is very small (<20 vol.%) relative to the voluminous oceanic lithosphere (Schwartz et al., 2001). The serpentinite bodies are located along detachments and constitute a large volume of the eastern boundary of the massif (Angiboust et al., 2012; Schwartz et al., 2001). The Monviso ophiolite corresponds to the subduction channel (Guillot et al., 2009).

3. Sampling strategy

The Chenaillet–Queyras–Monviso transect is a unique natural laboratory for observing mineral changes in serpentinite along an increasing metamorphism gradient. However, there are no directly applicable thermal calibrations in serpentinites; therefore, we propose to estimate the thermal conditions by applying the method of Raman spectroscopy of carbonaceous material (RSCM) to the metasediments associated with the serpentinites to obtain the T_{max} experienced by the serpentinites. A thermal transect is realized, according to 25 metasediment samples from the Chenaillet to the Monviso (Fig. 1a, Table 1). These sediments are Cretaceous calcschists derived from foraminifera oozes (Deville et al., 1992). The lithology of each sample is not homogeneous due to variation in carbonate-clay proportions. Moreover, the carbonate contents result both from biogenic production (pelagic foraminifera) and from detrital input (calciturbidites). The samples are strongly deformed, and the main schistosity is dominated by phengite, quartz, calcite and oxides. Glaucophane and pseudomorphs of lawsonite and zoisite are also present. Along this thermal transect, 8 serpentinites have been studied (Fig. 1a). The serpentinite samples were taken from the cores of hecto-metric serpentinite bodies; these bodies (100 m) were embedded in the metasediments from which the metasediment samples were acquired. These serpentinites escaped alpine deformations and preserved oceanic mesh textures. Sample ICH2 comes from the ophiolitic Chenaillet massif. This sample records a low degree of metamorphic conditions, with sea-floor metamorphism (Mével et al., 1978) overprinted by sub-greenshist facies conditions (P<4 kbar; T~200–300 °C; Goffé et al., 2004) related to alpine metamorphism. Sample CR02 comes from the Cristillan massif at the western boundary of the Schistes lustrés complex in the LT-blueschist domain (Fig. 1). Two samples come from the medium-temperature blueschist domain (MT-blueschist) of the Schistes lustrés complex: RQ23 from the Rocca Nera massif and RQ16 from the Eychassier massif. Samples BB01 (Bric Bouchet massif) and RQ01 (Traversette massif) come from the HT-blueschist domain of the Schistes lustrés complex. The samples Vi01 and Vi02 come from the Monviso eclogitic ophiolite.

4. Temperature estimates from Raman spectroscopy of carbonaceous material (RSCM)

4.1. Analytical conditions

Raman spectroscopy on carbonaceous material (RSCM) is based on the quantitative degree of graphitization of the organic material during regional metamorphic processes. The graphitization phenomenon corresponds to the solid-state transformation of organic matter into carbonaceous material. The structure of carbonaceous matter is not sensitive to the retrograde history related to the exhumation of metamorphic rocks. The progressive graphitization process can be used to estimate the peak temperature (T_{max}) reached by a given sample (Beyssac et al., 2002, 2003). The degree of graphitization appears to be independent of the metamorphic pressure, although a minimum pressure is required for the graphitization process to take place (Quirico et al., 2009). This thermometer is based on the quantification of the degree of ordering of the carbonaceous material, using the R2 area ratio between the G, D1 and D2 bands ($R2 = D1/[G + D1 + D2]$)) extracted from the Raman spectra (Beyssac et al., 2002). The R2 ratio is linearly correlated with the T_{max} of the metamorphic cycle ($T_{max}(°C) = -445 \times R2 + 641$). This correlation may be used as a thermometer with an intrinsic error calibration of 50 °C due to the petrological data used for calibration and a precision of approximately 15 °C (Beyssac et al., 2007).

Raman spectroscopy was performed at the ENS-Lyon using a Horiba Jobin-Yvon LabRam HR800 apparatus. The excitation was provided by an argon laser with a wavelength of 514 nm. An Olympus™ BX30 open microscope equipped with a ×100 objective lens was

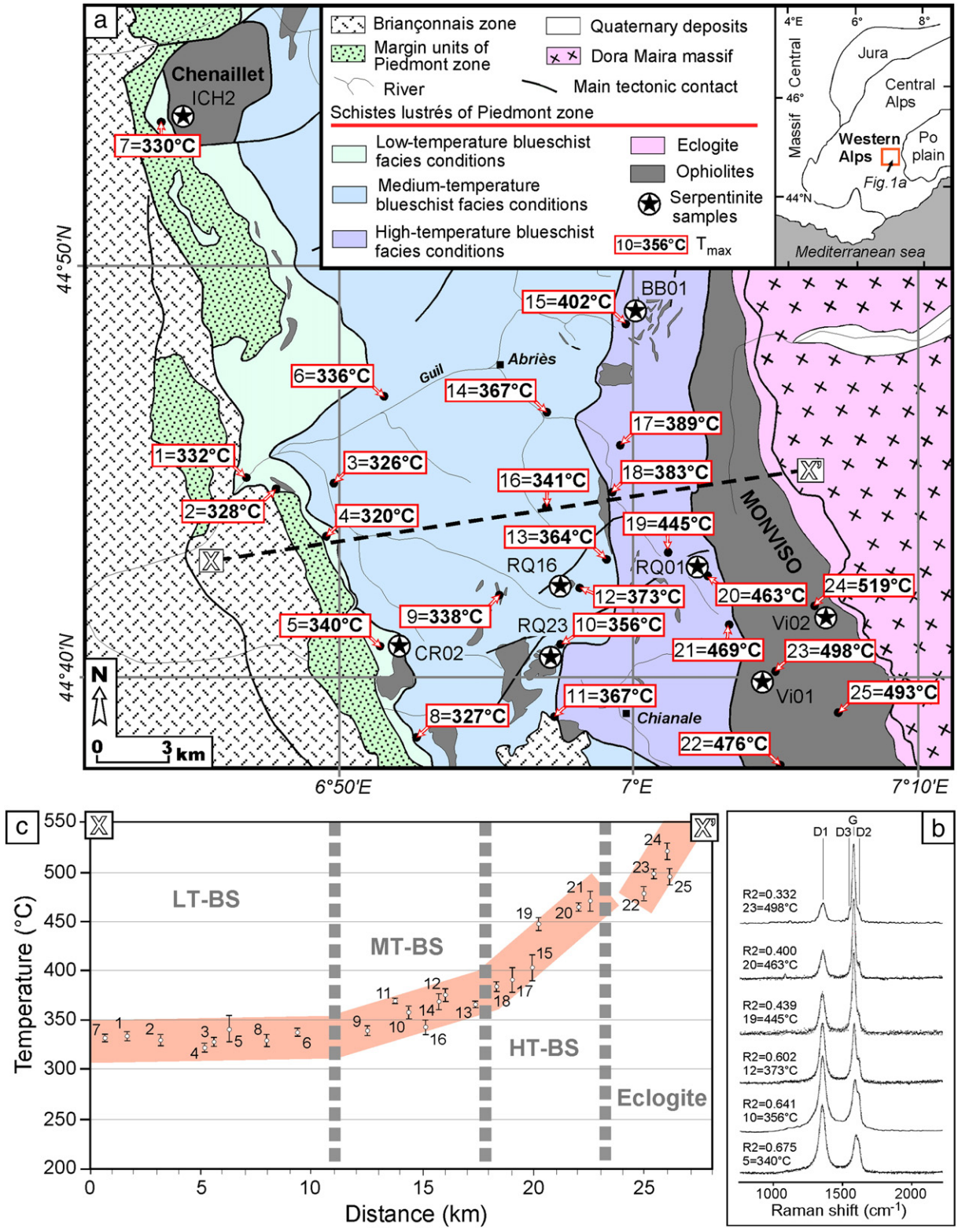

Fig. 1. (a) Tectonic sketch map of the southwestern Alps, and T_{max} results of metasediments obtained by the RSCM method. Seven serpentinites were sampled along the paleo-subduction zone from sub-greenschist (Chenaillet) to eclogitic (Monviso) facies conditions. (b) Characteristic evolution of Raman spectra from selected metasediments. Positions of the graphite G band and D1, D2, D3 defect bands are indicated. For each spectrum, the value of the mean R2 ratio (R2 = D1/[G + D1 + D2] peak area ratio) is given (see Table 1). (c) T_{max} results projected onto a WSW – ENE cross section (XX′).

coupled to the spectrometer to focus the laser beam onto an area that was 1 μm in diameter. The backscatter of the Raman signal was collected. The acquisition duration was approximately 120 s distributed over two accumulating cycles, with a laser power of approximately 700 μW at the sample surface. The signal was dispersed using a 1800 lines/mm grating. The Raman spectrometer was calibrated

Table 1
RSCM results with longitude (Long.) and latitude (Lat.) in decimal degrees (WGS84), number of Raman spectra (n), R2 ratio (mean and standard deviation) and T_{max} (mean and 1-σ uncertainty).

Sample number	Long. (N)	Lat. (E)	n	R2		T_{max} (°C)	
				Mean	Std	Mean	1σ
Queyras Schistes lustrés low-temperature blueschist							
1	44.7578	6.7918	10	0.694	0.019	332.3	8.33
2	44.7109	6.8138	10	0.703	0.024	328.3	10.47
3	44.7526	6.8432	9	0.707	0.021	326.5	9.55
4	44.7255	6.8432	9	0.722	0.021	317.6	9.28
5	44.6801	6.8702	13	0.675	0.036	340.5	15.95
6	44.7848	6.8784	14	0.686	0.017	335.9	7.44
7	44.8904	6.7233	9	0.700	0.020	330.0	6.70
8	44.6413	6.8942	8	0.707	0.026	326.7	11.88
9	44.6738	6.9405	10	0.683	0.020	337.5	8.94
Queyras Schistes lustrés medium-temperature blueschist							
10	44.6753	3.9906	11	0.641	0.027	355.9	11.94
11	44.6443	6.9929	12	0.616	0.036	367.5	4.45
12	44.7013	7.0048	11	0.602	0.027	373.1	12.05
13	44.7410	7.0288	11	0.622	0.015	364.3	6.45
14	44.7783	6.9783	7	0.615	0.035	367.5	15.57
16	44.7389	6.9679	13	0.673	0.032	341.3	14.39
Queyras Schistes lustrés high-temperature blueschist							
15	44.8147	7.0288	11	0.537	0.052	401.9	23.16
17	44.7586	7.0343	6	0.566	0.079	388.9	22.58
18	44.7350	7.0310	11	0.581	0.022	382.6	9.87
19	44.7117	7.0705	10	0.439	0.028	445.5	12.44
20	44.7010	7.0996	12	0.400	0.022	462.8	9.67
21	44.6881	7.1162	10	0.386	0.044	469.1	19.78
Monviso eclogite							
22	44.5953	7.1467	10	0.371	0.033	475.9	14.00
23	44.6508	7.0803	11	0.321	0.020	489.2	9.10
24	44.6939	7.1549	12	0.273	0.037	519.5	16.35
25	44.6426	7.1771	6	0.332	0.036	493.3	16.00

with a silicon standard. For each sample, 6 to 13 spectra were recorded (noted 'n' in Table 1). The baseline correction, peak position, and band width were determined using the Peakfit© software.

4.2. T_{max} results

From west to east, the Raman spectra show a decrease of the D1 peak area associated with a decrease in the width of the G band, resulting in a decrease in the R2 ratio (Fig. 1b). This trend in the R2 ratio is compatible with a T_{max} increase in the metamorphic samples (Beyssac et al., 2007; Lanari et al., 2012). The T_{max} estimates by RSCM thermometry range from 330 ± 20 °C to 520 ± 20 °C (Table 1). The projection of the estimated T_{max} along a WSW to ENE profile (XX′ in Fig. 1c) shows a progressive increase of T_{max}. This increase in temperature is compatible with the metamorphic gradient already proposed by Tricart and Schwartz (2006) in the studied area. The temperature increase from west to east is also consistent with the increase in pressure along a low-temperature subduction-related geothermal gradient (Angiboust et al., 2012; Goffé et al., 2004; Lardeaux et al., 2006). This relationship allows us to associate a pressure maximum with the T_{max} estimated by RSCM. The sub-greenschist facies domain of the Chenaillet massif corresponds to a P–T range of P<4 kbar and T~200–300 °C. The LT-blueschist domain corresponds to P–T conditions of P = 9–11 kbar and 320<T<360 °C; the MT-blueschist domain indicates P–T conditions of 10–12 kbar and 340–390 °C; the HT-blueschist domain corresponds to P–T conditions of 12<P<15 kbar and 380<T<470 °C; and the eclogitic domain indicates conditions of 20<P<26 kbar and 480<T<520 °C.

5. XRD characterization of serpentinites

5.1. Experimental conditions

A <2 mm fraction of each serpentinite sample was powdered using a McCrone micronizing mill and washed with H_2O. The resulting slurry was centrifuged and freeze-dried before being prepared as a randomly oriented mount. The XRD patterns were recorded with a Bruker D5000 powder diffractometer equipped with a SolX Si(Li) solid state detector from Baltic Scientific Instruments using CuKα 1 + 2 radiation. The intensities were recorded at 0.04° 2-theta step intervals from 5 to 90° (5 s counting time per step) for bulk serpentinite mineralogy determination. The XRD detection level was approximately one percent (<1%).

5.2. Results

The XRD results and the mineralogical assemblages are presented in Fig. 2 and Table 2. All of the XRD lines of the samples are dominated by serpentine minerals (serpentine species > 90%) associated with magnetite (Fig. 2). Brucite was not observed; however, mineral species are not detected below a concentration of 1 wt.%. The serpentinite sampled in the Chenaillet massif (ICH2) is composed of serpentine, magnetite, chlorite and rare magmatic clinopyroxene. The serpentinites sampled in the LT-blueschist (CR02) and MT-blueschist (RQ23 and RQ16) domains present mineralogical assemblages dominated by serpentine and minor magnetite. In Sample RQ16, chlorite was detected. The serpentinites from the HT-blueschist (BB01 and RQ01) and eclogitic (Vi01) domains are composed of serpentine, metamorphic olivine and magnetite. The mineral antigorite is detectable in the XRD spectrum of Sample BB01 (Fig. 2 and Table 2). The presence of olivine is related to the onset of antigorite destabilization during the dehydration reaction (Evans, 2004). This secondary olivine appears in Samples RQ01 and Vi01. In Sample Vi01, clinopyroxene and chlorite are detected, in accordance with the microscopic observations (Auzende et al., 2006). To precisely identify the varieties of serpentines, we used Raman spectroscopy coupled with microscopic observations.

6. Serpentine characterizations

6.1. Raman spectrometry

The different serpentine species have been characterized by Raman spectroscopy coupled with petrographic observations of polished thin-sections of serpentinites. The Raman signal was acquired over approximately 90 s in three accumulating cycles, with a laser output power on the sample surface adjusted between 10 and 20 mW. The spectral resolution was 1 cm^{-1} using 1800 lines/mm grating. A reproducibility of 1 cm^{-1} was attained on successive spectra of a given mineral sample. The spectral regions from 150 to 1150 cm^{-1} and from 3600 to 3720 cm^{-1} were investigated because they include the lattice vibrational modes and the OH stretching mode region that is characteristic of serpentine species (Auzende et al., 2004; Groppo et al., 2006; Rinaudo et al., 2003).

The bands detected in these spectral regions are indicative of the crystalline structure of the sample. For each spectrum, the assignment of the band position and the full width at half maximum were determined using the Peakfit© software.

In the low wavenumber region, four main peaks (near 230, 390, 690 and 1100 cm^{-1}) characterize the spectra of lizardite and chrysotile (Fig. 3a). Intense peaks specific to the antigorite spectrum occur at lower wavenumbers (226, 373, 680 and 1043 cm^{-1}) and are much broader than those corresponding to other serpentines (Fig. 3b). The differences between chrysotile and lizardite spectra, although small, can be clearly identified by the sharpness of the Raman lines.

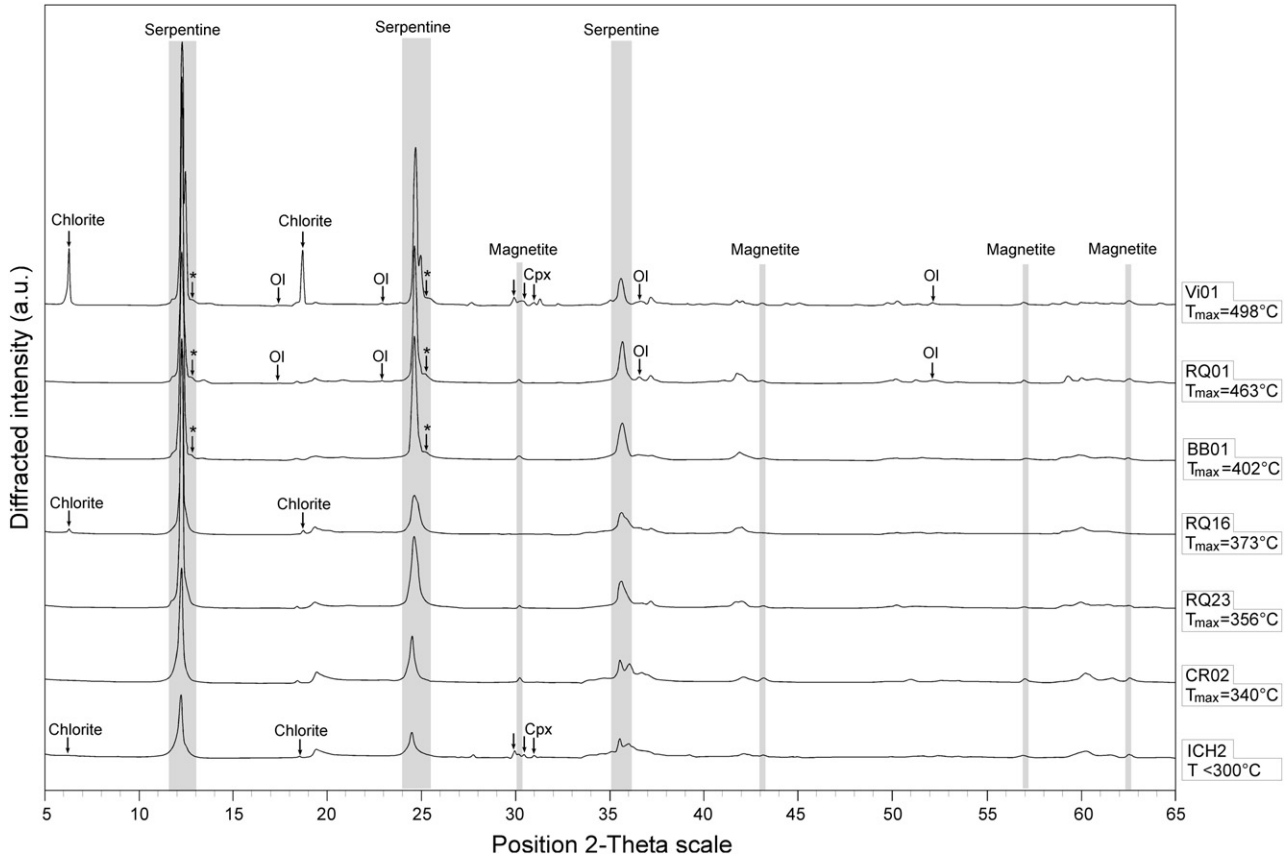

Fig. 2. XRD patterns of serpentinites. The mineralogy is dominated by a magnetite and serpentine assemblage. The antigorite peaks (black star) and olivine (Ol) appear in samples RQ01 and Vi01. The presence of olivine is due to the onset of antigorite destabilization into olivine.

In particular, a single band at 1100 cm^{-1} is observed in chrysotile, whereas several convoluted bands are observed between 1060 and 1100 cm^{-1} in lizardite (Fig. 3a). In the high wavenumber region, the convoluted vibrational modes attributed to the OH stretching of serpentine are located between 3600 and 3720 cm^{-1}. In chrysotile, the most intense band occurs at 3697 cm^{-1}, with a distinct shoulder at 3690 cm^{-1} and a weak band at 3648 cm^{-1}. Lizardite has a markedly different spectrum (Fig. 3a): the most intense band occurs at a lower frequency (minimum at 3680 cm^{-1}) with a well-defined high frequency band at 3703 cm^{-1}. In antigorite, the spectra are characterized by a broad band at 3670 cm^{-1} and a sharp band at 3700 cm^{-1} (Fig. 3b). Mixed lizardite/antigorite spectra are also observed (Fig. 3c). In the low wavenumber region, the peak at 1043 cm^{-1} is present (as in antigorite), but the peak at 373 cm^{-1} is shifted to ~380 cm^{-1} (toward the classical ~390 cm^{-1} peak of lizardite). In the high wavenumber region, the second "antigorite" peak at 3700 cm^{-1} is still present, but the most intense peak is located between 3670 cm^{-1} and 3680 cm^{-1}, in an intermediate position between the most intense "antigorite" and "lizardite" peaks (Fig. 3c).

6.2. Petrology

The distribution of the serpentine species correlates with the T_{max} along the XX′ profile (Fig. 1c). Lizardite dominates in the greenschist and LT-blueschist facies (from<300 °C to 360 °C), while antigorite progressively appears in the LT-blueschist facies. Antigorite becomes progressively dominant in the MT-blueschist facies (340–390 °C), ultimately becoming the sole serpentine species in the HT-blueschist and eclogite facies (T>380 °C). Chrysotile is observed in all of the high pressure serpentinite samples, filling in the late cracks or micro-fractures related to final exhumation at the ductile/brittle transition. In the following paragraphs, we detail the mineralogy and texture of the serpentinites according to the degree of metamorphism. The T_{max} for each serpentinite sample refers to the T_{max} estimated from the associated metasediments.

Sample ICH2 (T<300 °C, according to Goffé et al., 2004) is characterized by the development of a mesh texture outlined by magnetite, which suggests the classical reaction of olivine + water = serpentine

Table 2
Mineral assemblage of the studied serpentinites as detected by XRD, with (+ + +) major phase, (+) minor phase (<10%), and (−) absent or below detection limit (<1%). Facies metamorphic conditions and T_{max} are also given. The black star indicates the presence of antigorite.

Sample	ICH2	CR02	RQ23	RQ16	BB01	RQ01	Vi01
facies	sub-GS	LT-BS	LT-BS	LT-BS	HT-BS	HT-BS	eclogite
T_{max}	~200–300 °C	340 °C	356 °C	373 °C	402 °C	463 °C	498 °C
Serpentine	(+++)	(+++)	(+++)	(+++)	(+++)*	(+++)*	(+++)*
Magnetite	(+)	(+)	(+)	(+)	(+)	(+)	(+)
Chlorite	(+)	(−)	(−)	(+)	(−)	(−)	(+)
Cpx	(+)	(−)	(−)	(−)	(−)	(−)	(+)
Olivine	(−)	(−)	(−)	(−)	(−)	(+)	(+)

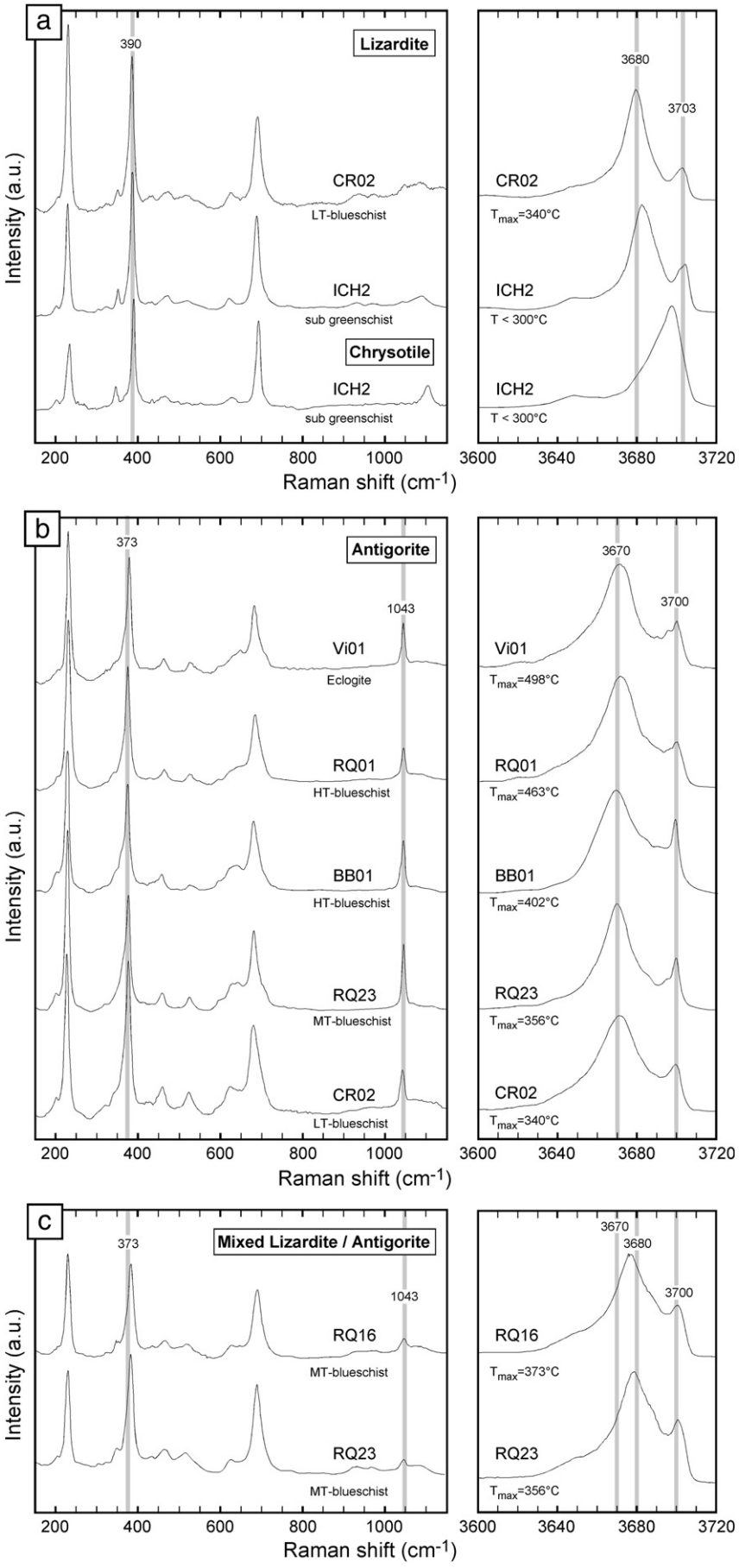
a
Lizardite
390
3680
3703
CR02
LT-blueschist
CR02
T_max=340°C
ICH2
sub greenschist
ICH2
T < 300°C
Chrysotile
ICH2
sub greenschist
ICH2
T < 300°C
Intensity (a.u.)
200 400 600 800 1000
3600 3640 3680 3720
Raman shift (cm-1)
b
Antigorite
373
1043
3670
3700
Vi01
Eclogite
Vi01
T_max=498°C
RQ01
HT-blueschist
RQ01
T_max=463°C
BB01
HT-blueschist
BB01
T_max=402°C
RQ23
MT-blueschist
RQ23
T_max=356°C
CR02
LT-blueschist
CR02
T_max=340°C
Intensity (a.u.)
200 400 600 800 1000
3600 3640 3680 3720
Raman shift (cm-1)
c
Mixed Lizardite / Antigorite
373
1043
3670
3680
3700
RQ16
MT-blueschist
RQ16
T_max=373°C
RQ23
MT-blueschist
RQ23
T_max=356°C
Intensity (a.u.)
200 400 600 800 1000
3600 3640 3680 3720
Raman shift (cm-1)

(mesh) + magnetite ± brucite (Fig. 4a and a′). The Raman spectrometry shows that lizardite is the dominant serpentine species (Fig. 3a). Locally, the mesh is crosscut by secondary chrysotile veins.

Sample CR02 (T_{max} = 340 °C) shows a mesh texture consisting of lizardite surrounded by magnetite (Fig. 4b and b′). Locally, secondary antigorite (representing less than 10% of the matrix) crystallized at the boundaries of relict brownish lizardite crystals. We assign the lizardite crystallization to the sea-floor metamorphism (oceanic serpentinization) and the antigorite crystallization to the LT-blueschist metamorphism.

Sample RQ23 (T_{max} = 356 °C) is composed equally of antigorite and relics of lizardite (Fig. 4c and c′). The antigorite crystallized at the grain boundaries of the lizardite relics and as millimeter-sized antigorite patches with an interlocking texture. The lizardite relics present the typical mixed lizardite-antigorite Raman spectra (Fig. 3c), suggesting the partial mineral replacement of oceanic lizardite by metamorphic micrometric antigorite. Magnetite locally outlines the original mesh texture.

Sample RQ16 (T_{max} = 373 °C) shows the same mineral relationships as sample RQ23, with some relics of lizardite that have a mixed character between antigorite and lizardite (Fig. 4d and d′). The antigorite that developed at the grain boundaries became enlarged and blades of antigorite crystallized. In this sample, the proportion of magnetite decreased, but chlorite crystallized (Fig. 2), which suggests the development of chlorite at the expense of magnetite and Al-rich lizardite (Table 3).

Sample BB01 (T_{max} = 402 °C), coming from the HT-blueschist unit, is composed only of antigorite and a string of magnetite that outlines the previous oceanic mesh texture (Fig. 5a and a′). The patches are composed of sub-millimetric interlocking blades of antigorite. The presence of antigorite is readily detectable in the XRD spectra (Fig. 2).

In Sample RQ01 (T_{max} = 463 °C), only antigorite serpentine is observed (Fig. 5b and b′). The mesh, still underlined by magnetite and bastite (free of magnetite), remains preserved, which suggests a static crystallization of antigorite at the expense of oceanic lizardite. The olivine peak appears in the XRD spectra.

In Sample Vi01 (T_{max} = 498 °C), antigorite is again the sole serpentine species (Fig. 5c and c′). Similar to Sample RQ01, the pseudomorphic texture (mesh and bastite) is preserved and underlined by magnetite, but antigorite blades of a few hundred microns have started to obliterate the mesh texture. In this sample, we observed olivine and chlorite signals in the XRD spectra (Fig. 2).

Sample Vi02 (T_{max} = 519 °C) is a sheared sample showing the crystallization of metamorphic olivine in C-planes at the expense of brucite and antigorite (Fig. 5d and d′).

6.3. Electron microprobe

In addition, the major element concentrations of the serpentine species were acquired using a Cameca SX100 electron microprobe at the "Laboratoire Magma et Volcans" (Clermont Ferrand, France). The operating conditions were as follows: an accelerating voltage of 15 kV, a sample current of 15 nA and a counting time of 10 s/element, except for Ni (20 s). The standards used were albite (Na), forsterite (Mg), orthoclase (K), wollastonite (Ca and Si), $MnTiO_3$ (Ti and Mn), Cr_2O_3 (Cr), fayalite (Fe), olivine (Ni), and synthetic Al_2O_3 (Al). Representative analyses are reported in Table 3. Serpentine phases can contain over 13 wt.% of water in their crystal structure. The volatile content (100% − wt.% major elements) in the different serpentine species is not always correlated with the degree of serpentinization because other phases (e.g., talc, brucite, chlorite, clay minerals) associated with serpentine minerals can influence this measurement. In the studied samples, the volatile content varies from 12.54 to 15.67 wt.% (Table 3). We did not observe any correlation between the volatile content in the serpentine minerals and the degree of metamorphism. However, we did observe a relationship between the homogeneity of the serpentine and the degree of metamorphism (Fig. 6). When plotted on the SiO_2 vs. Al_2O_3 field, the lower metamorphic samples are scattered suggesting the preservation of primary chemical signal of the pyroxene (Al_2O_3 and SiO_2 rich) and olivine (poor in Al_2O_3 and SiO_2), while the higher metamorphic samples are grouped closer to the end-member antigorite composition (Fig. 6), with 44 wt.% SiO_2 and 1.03 wt.% Al_2O_3 (Deer et al., 1992). This suggests that antigoritization enhances chemical homogenization and the excess in Al_2O_3 allow chlorite to crystallize (Fig. 2). The samples with an intermediate degree of metamorphism, dominated by mixed lizardite/antigorite, fall between the lizardite and antigorite fields. It is also noticeable that the Al_2O_3 content decreases and the SiO_2 content increases with the degree of metamorphism (Fig. 6). This increase of SiO_2 in serpentine is correlated with a slight increase of whole-rock SiO_2 content, from ~39.4 wt.% in the sub-greenschist serpentinites (Chenaillet massif) to ~40.5 wt.% in the eclogitic serpentinites (Monviso ophiolite) (Lafay et al., in press).

7. Discussion

7.1. Lizardite to antigorite transitions

The aim of this study is to develop a combined mineral investigation of serpentinites and compare the results with T_{max} estimates from associated metasediments. This approach allows us to indirectly constrain the P–T conditions of the phase changes in natural serpentinites and to compare our results with previous experimental works. Moreover, most of the published results concerning the changes from lizardite/chrysotile to antigorite are acquired through experiments performed at intermediate pressures of 6–7 kbar (e.g., O'Hanley, 1996) but in natural samples, antigorite crystallized in veins at minimum pressure of 1–2 kbar (Viti and Mellini, 1996); our samples allow us to characterize this transition at higher pressures (between 4 and 26 kbar) that are pertinent to the P–T conditions in subduction zones. Our study highlights the following important points:

1. —The early serpentinization stage is related to the hydrothermalism of the oceanic lithosphere and generates lizardite-bearing mesh textures (Fig. 7a and b).
2. —In the lowest-grade metamorphic units (sub-greenschist facies; P<4 kbar; T~200–300 °C), antigorite is absent and lizardite is the dominant phase. Such observations are in agreement with previous experimental results (e.g., Evans, 2004).
3. —In polymetamorphic weakly deformed domains, the oceanic mesh textures are preserved in all peak P–T conditions (Fig. 7b). At the initial stages, antigorite appears along the lizardite grain boundaries (Fig. 7c) and at more evolved stages overprints lizardite (Fig. 7d), preserving the initial textures (mesh and bastite). This observation argues against the commonly proposed idea that antigorite preferentially crystallizes within deformed domains (Miyashiro et al., 1969).
4. —Antigorite crystallizes in two distinct crystal locations. Antigorite first appears in LT-blueschist at 320 °C at the lizardite grain boundary, forming a network of veins (Fig. 7c). These veins grow with the degree of metamorphism, from ~20 μm up to 150 μm (Fig. 7d) in the MT-blueschist facies (up to 390 °C). Such crystallization

Fig. 3. Raman spectra acquired from different varieties of serpentine from the study area in low frequency (150–1150 cm^{-1}) and OH stretching (3600 to 3720 cm^{-1}) ranges. The characteristic bands of antigorite (373, 1043, 3670 and 3700 cm^{-1}) and lizardite (390, 3680, 3703 cm^{-1}) are indicated in grey. (a) Raman spectra of lizardite and chrysotile. (b) Raman spectra of antigorite related to the T_{max}. (c) Raman spectra of mixed lizardite/antigorite serpentine.

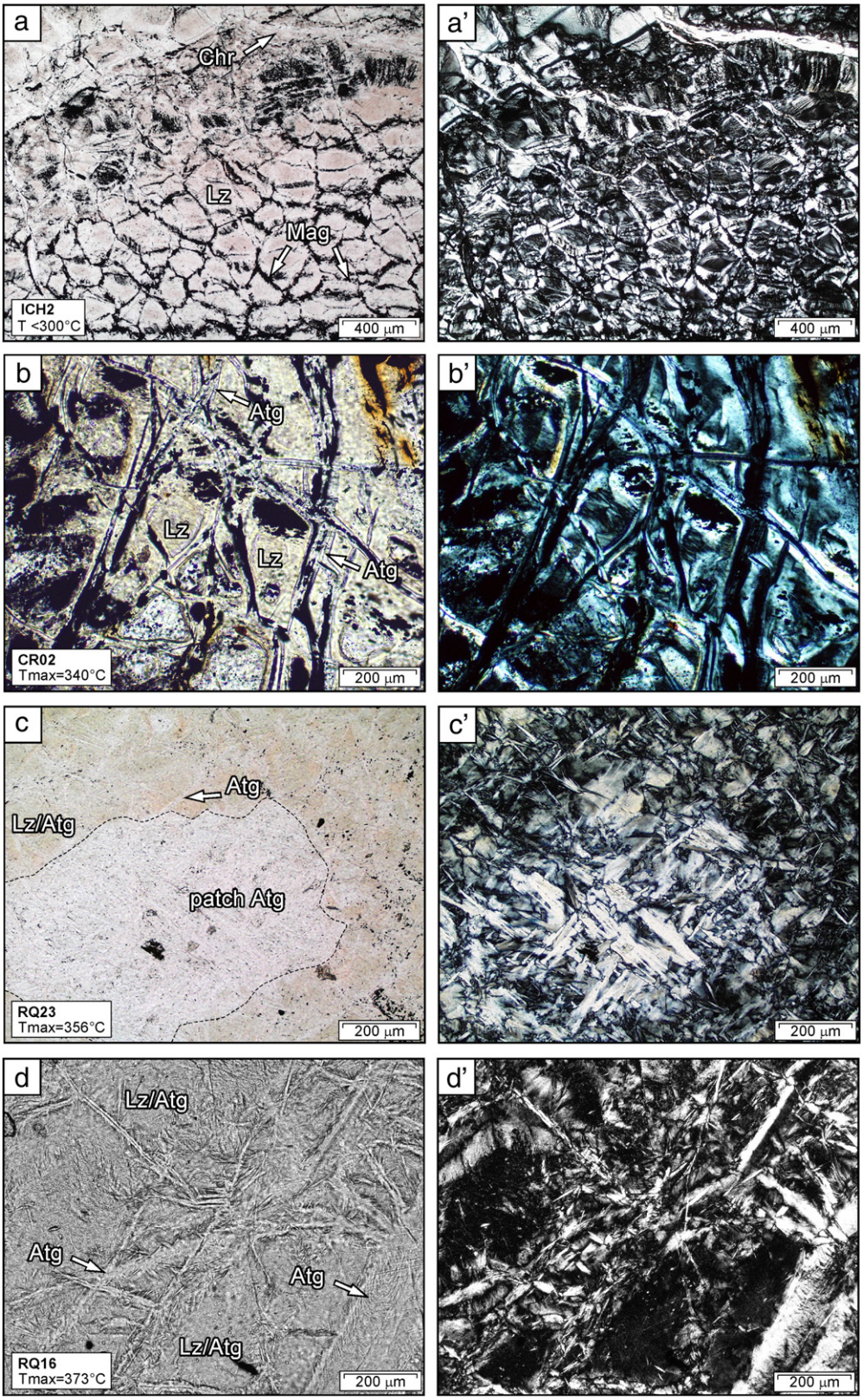

Fig. 4. Photomicrographs of characteristic textures of serpentinite from the study area: Atg, antigorite; lz, lizardite; Chr, chrysotile; Mag, magnetite; x, polarized light; x′, crossed-polarized light. The T_{max} obtained from the associated metasediments is also indicated. (a–a′). Sample ICH2 (Chenaillet massif). Mesh texture developed from olivine is observed in locations where lizardite is the only developed serpentine species. At the top of the image, secondary veins infilled by chrysotile cross-cut the mesh texture. (b–b′). Sample CR02 comes from the low-temperature blueschist domain (Cristillan massif). The sample is dominated by mesh texture underlined by lizardite. Secondary antigorite crystallized at the boundary of the lizardite minerals. In the antigorite zone, relics of lizardite (brownish minerals) are still present. (c–c′). Sample RQ23 comes from medium-temperature blueschist domain (Rocca Bianca massif). The sample is equally dominated by lizardite and antigorite. In the lizardite-dominant zone (greenish color), the mesh texture is partly preserved; however, antigorite developed at the expense of lizardite at the grain boundaries. Antigorite minerals with interlocked microstructures also form millimeter-sized patches that are free of lizardite relics. (d–d′). Sample RQ16 comes from the intermediate-temperature blueschist domain (Refuge du Viso). The sample is dominated by antigorite minerals, which are developed in a dense network of veins at the expense of lizardite preserved in mesh texture.

Table 3
Representative microprobe analyses of serpentine minerals from alpine serpentinites. All values are in wt.% (b.d.l. = below detection limit; n.d. = not determined).

Sample	ICH2	ICH2	ICH2	ICH2	ICH2	ICH2	ICH2	CR02	CR02	CR02	CR02	CR02	CR02	CR02	RQ23	RQ23	RQ23	RQ23	RQ23	RQ23	RQ23	RQ23	RQ23
Sample nb	# 1	#2	# 3	# 4	# 5	# 6	# 7	# 8	# 9	# 10	# 11	# 12	# 13	# 14	# 15	# 16	# 17	# 18	# 19	# 20	# 21	# 22	# 23
minerals	Lz	Lz	Lz	Lz	Lz	Lz	Lz	Lz	Lz	Lz	Lz	Lz	Lz	Lz	Lz/Atg	Lz/Atg	Lz/Atg	Lz/Atg	Atg	Atg	Atg	Atg	Atg
Facies	Sub-greenschist							LT-Blueschist								MT-Blueschist							
T_{max}	~200–300 °C							340 °C								356 °C							
All element in %																							
SiO_2	40.28	41.97	40.71	43.79	42.47	42.91	41.68	40.35	43.15	38.71	43.00	42.79	40.06	40.45	42.35	42.23	41.76	42.87	43.98	44.27	43.08	43.85	43.82
TiO_2	0.11	0.10	0.13	0.00	0.03	0.02	0.13	0.04	0.04	0.03	0.02	0.03	0.05	b.d.l.	0.01	b.d.l.	0.05	0.03	0.01	0.01	b.d.l.	b.d.l.	0.01
Al_2O_3	3.88	2.08	4.31	0.89	0.52	0.78	2.27	2.54	1.06	4.71	0.72	0.58	3.65	2.55	0.75	2.74	1.20	0.69	0.40	0.25	0.72	0.37	0.46
Cr_2O_3	1.11	1.18	1.28	0.03	0.01	0.06	0.64	1.06	0.10	1.45	0.08	0.01	1.23	0.07	0.17	0.31	0.05	0.29	0.01	0.02	1.09	0.00	0.50
MgO	34.21	36.83	33.06	38.11	39.37	39.3	37.14	35.93	38.7	34.92	40.33	39.46	34.14	37.29	38.16	36.48	37.03	37.12	37.82	37.59	37.54	36.98	38.12
FeO	3.75	3.38	3.64	2.40	2.56	2.93	3.46	4.61	2.73	4.21	3.46	3.79	4.09	4.61	5.65	4.99	5.65	5.23	4.52	4.77	4.96	5.51	4.18
MnO	0.13	0.13	0.09	0.14	0.11	0.03	0.10	0.10	0.03	0.08	0.02	0.05	0.10	0.07	0.03	0.10	0.06	0.08	0.07	0.14	0.08	0.15	0.11
NiO	0.10	0.04	0.04	0.11	0.30	0.10	0.08	0.14	0.24	0.09	0.25	0.25	0.06	0.18	0.22	0.19	0.21	0.24	0.24	0.24	0.24	0.19	0.23
CaO	1.04	0.21	1.99	0.33	0.09	0.06	0.18	0.06	0.07	0.09	0.04	0.03	0.09	0.06	0.01	0.04	0.03	b.d.l.	b.d.l.	b.d.l.	b.d.l.	0.01	b.d.l.
Na_2O	0.02	0.01	0.01	0.01	0.03	b.d.l.	0.02	b.d.l.	b.d.l.	0.02	0.04	0.03	0.04	0.03	b.d.l.	0.02	0.01	b.d.l.	b.d.l.	0.05	b.d.l.	b.d.l.	b.d.l.
K_2O	0.01	0.02	0.03	0.01	0.05	0.02	b.d.l.	0.02	0.01	0.01	0.01	0.01	0.03	0.02	0.01	b.d.l.	0.02	0.02	b.d.l.	0.03	b.d.l.	0.03	0.02
Total	84.63	85.94	85.30	85.82	85.54	86.20	85.70	84.86	86.13	84.33	87.96	87.03	83.55	85.34	87.36	87.11	86.06	86.57	87.05	87.36	87.70	87.11	87.46
Volatile	15.37	14.06	14.70	14.18	14.46	13.80	14.3	15.14	13.87	15.67	12.04	12.97	16.45	14.66	12.64	12.89	13.94	13.43	12.95	12.64	12.30	12.89	12,54

Sample	RQ16	RQ16	RQ16	RQ16	RQ16	RQ16	RQ16	RQ16	RQ16	BB01	BB01	BB01	RQ01	RQ01	RQ01	RQ01	RQ01	Vi01	Vi01	Vi01	Vi01	Vi01	Vi01
Sample nb minerals	# 24	# 25	# 26	# 27	# 28	# 29	# 30	# 31	# 32	# 33	# 34	# 35	# 36	# 37	# 38	# 39	# 40	# 41	# 42	# 43	# 44	# 45	# 46
	Lz/Atg	Lz/Atg	Lz/Atg	Lz/Atg	Lz/Atg	Lz/Atg	Lz/Atg	Lz/Atg	Lz/Atg	Atg	Atg	Atg	Atg	Atg	Atg	Atg	Atg	Atg	Atg	Atg	Atg	Atg	Atg
Facies	MT-Blueschist									HT-Blueschist			HT-Blueschist					Eclogite					
T_{max}	373 °C									402 °C			463 °C					498 °C					
All element in %																							
SiO2	40.76	41.17	42.63	41.54	41.46	42.42	40.86	41.83	41.87	43.49	43.37	43.14	42.81	42.51	43.51	44.29	43.11	43.68	42.10	43.83	43.43	42.80	43.41
TiO_2	0.02	0.07	0.05	0.03	b.d.l.	b.d.l.	0.04	b.d.l.	0.05	0.02	b.d.l.	0.02	b.d.l.	0.02	b.d.l.	b.d.l.	0.01	b.d.l.	0.04	b.d.l.	b.d.l.	b.d.l.	0.03
Al_2O_3	2.99	2.80	2.60	2.59	1.62	2.11	2.56	2.38	4.37	1.15	1.14	1.22	1.81	1.29	1.17	0.97	1.11	1.33	2.85	1.14	1.17	1.81	1.52
Cr_2O_3	0.52	0.68	0.48	0.16	0.22	0.10	0.63	0.6	1.03	0.28	0.75	0.54	0.39	0.88	0.57	0.38	0.42	0.07	0.22	0.18	0.29	0.51	1.60
MgO	34.25	34.19	34.21	35.44	35.41	33.26	34.75	35.21	32.64	39.63	39.67	38.96	38.67	39.4	39.05	39.42	39.7	38.23	37.41	38.17	38.25	37.98	38.46
FeO	7.64	6.34	6.78	5.43	6.9	5.41	7.23	7.05	6.87	2.16	2.16	1.87	2.74	2.04	1.89	2.07	2.22	3.49	3.61	3.05	3.38	3.13	3.38
MnO	0.12	0.13	0.12	0.03	0.11	0.10	0.09	0.09	0.11	0.17	0.07	0.06	0.09	0.11	0.14	0.10	0.13	0.03	0.01	b.d.l.	0.05	b.d.l.	0.05
NiO	0.12	0.12	0.14	0.13	0.14	0.14	0.11	0.11	0.11	0.09	0.10	0.09	0.10	0.11	0.09	0.10	0.07	0.14	0.11	0.02	0.02	0.01	0.03
CaO	0.08	0.23	0.16	0.09	0.06	0.15	0.09	0.04	0.22	0.01	b.d.l.	0.03	b.d.l.	b.d.l.	0.01	0.02	b.d.l.	0.01	0.02	b.d.l.	b.d.l.	0.02	0.01
Na_2O	b.d.l.	b.d.l.	b.d.l.	b.d.l.	0.01	b.d.l.	0.01	b.d.l.	0.05	0.01	b.d.l.	b.d.l.	b.d.l.	0.01	b.d.l.	b.d.l.	0.03	b.d.l.	b.d.l.	b.d.l.	b.d.l.	b.d.l.	0.01
K_2O	0.02	b.d.l.	b.d.l.	0.01	b.d.l.	b.d.l.	0.02	0.01	0.02	0.01	0.02	0.04	0.03	0.02	b.d.l.	0.01	0.02	b.d.l.	0.04	b.d.l.	b.d.l.	0.01	0.02
Total	86.53	85.73	87.17	85.45	85.93	83.70	86.40	87.34	87.35	87.01	87.27	85.97	86.63	86.39	86.44	87.37	86.81	86.98	86.41	86.40	86.60	86.28	88.51
Volatile	13.47	14.27	12.83	14.55	14.07	16.3	13.60	12.66	12.65	12.99	12.73	14.03	13.37	13.61	13.56	12.63	13.19	13.02	13.59	13.60	13.40	13.72	11.49

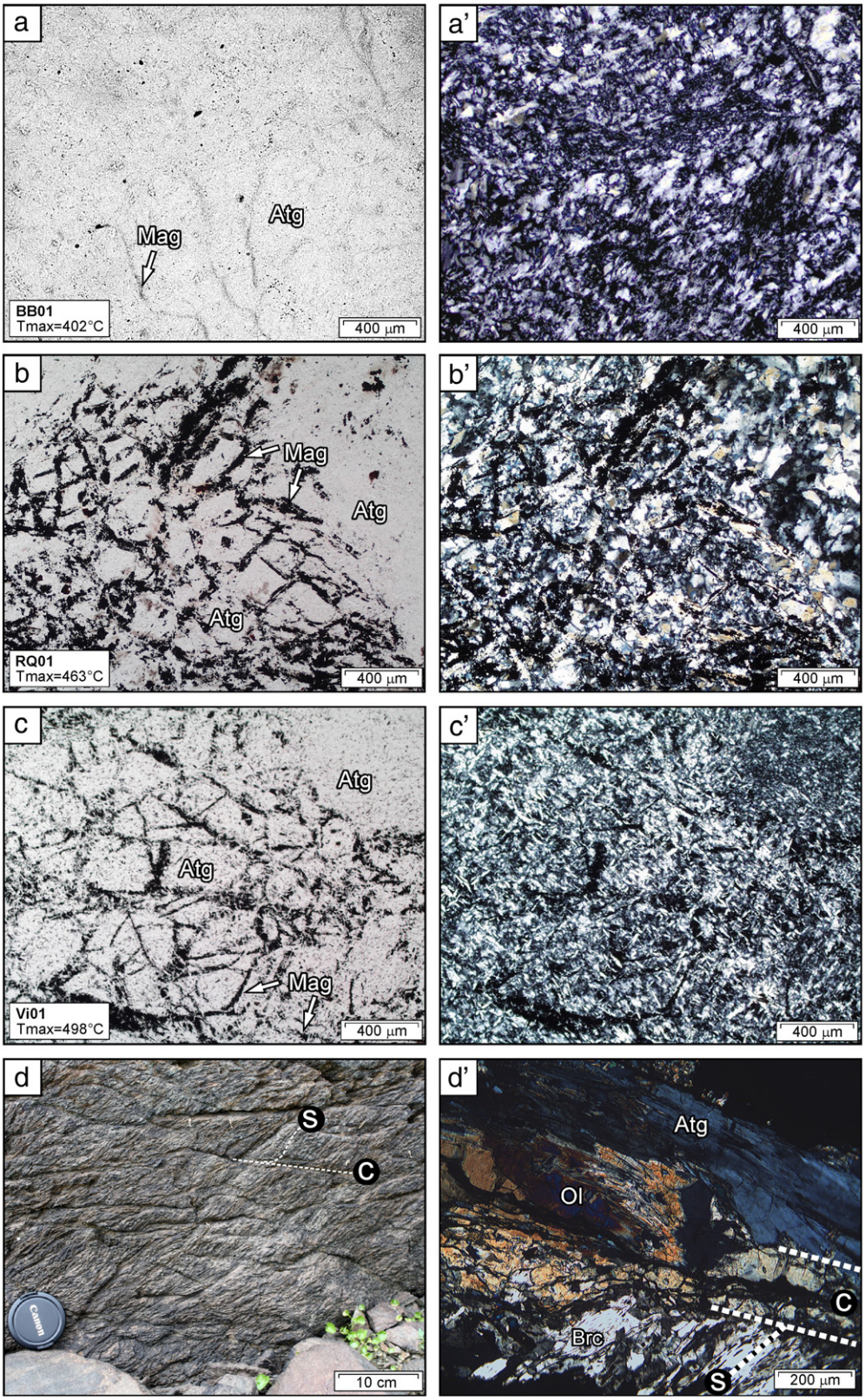

Fig. 5. Photomicrographs of characteristic textures of serpentine species from the western Alps: Atg, antigorite; Lz, lizardite; Chr, chrysotile; Mag, magnetite; x, polarized light; x′, crossed-polarized light. The T_{max} obtain on the associated metasediments is also indicated. (a–a′). Sample BB01 comes from the high-temperature blueschist domain (Bric Bouchet massif). This sample is dominated by antigorite. The magnetite underlines the early mesh structure. (b–b′). Sample RQ01 comes from the high-temperature blueschist domain (Traversette massif). In this sample, only antigorite is observed. Mesh and bastite textures are well preserved, suggesting a static crystallization of antigorite, most likely at the expense of early lizardite produced during ocean floor metamorphism. (c–c′). Sample Vi01 comes from Monviso eclogitic ophiolite. The antigorite is the only serpentinite species that preserves the mesh texture underlined by magnetite. (d–d′). Sample Vi02 comes from Monviso eclogitic ophiolite. As the outcrop scale C-S structures are well observed. In this section, C-plane is underlined by secondary olivine while S-planes are underlined by brucite and antigorite. This susggests that olivine crystallized at the expense of brucite + antigorite according to the Reaction (4) (see text for discussion).

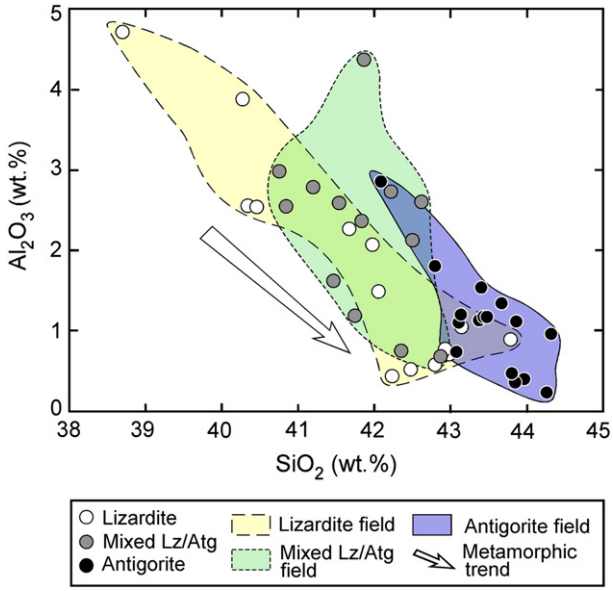

Fig. 6. Microprobe analyses (in wt.%) of serpentine samples plotted in an Al_2O_3 versus SiO_2 diagram (cf Table 3). The arrow indicates the metamorphic trend from sub-greenschist to eclogitic metamorphic facies conditions. The antigoritization processes in the serpentinites are characterized by a chemical homogenization associated with the increase in the metamorphic conditions.

texture is typical of mineral replacement by dissolution–precipitation processes in the presence of a free fluid (Lafay et al., 2012; Putnis, 2009).

The second crystal location is where antigorite crystallizes in the cores of lizardite grains in MT-blueschist facies conditions (Fig. 7d). Raman spectroscopy shows mixed lizardite/antigorite spectra, suggesting an intimate association of lizardite and antigorite at the micron-scale (Fig. 7a). A mixed spectrum of these two phases can simply occur during a partial replacement of one phase by another during dissolution-reprecipitation, which is commonly observed during pseudomorphism, especially if the minerals are very fine grained as is the case here (Putnis, 2009). The crystallization of antigorite at the expense of lizardite is partial between 340 and 380 °C and complete above in HT-blueschist and eclogitic facies conditions (Fig. 7a and e).

7.2. Lizardite to antigorite reactions

In the literature, it is typically proposed that the thermal stability fields of antigorite and lizardite theoretically overlap between temperatures of 30 and 300 °C, while chrysotile is metastable (e.g., Evans, 2004). We can refine the relative stability fields of lizardite and antigorite from our observations of high-pressure natural samples. It is well known that serpentinization is a complex process controlled by time- and site-dependent variables such as fluid/rock ratios, silica activity, oxygen fugacity and pH (Evans, 2004; Frost and Beard, 2007). Lizardite and antigorite coexist (or at least lizardite is not completely destabilized) between 320 and 390 °C for pressures greater than 9 kbar (Fig. 8). It is noticeable that below 300 °C and 4 kbar, antigorite is not observed. This observation contradicts the phase diagram of O'Hanley (1996), in which antigorite appears at 250 °C at low pressures, and suggests that antigorite crystallization is not only temperature dependent but also may be pressure dependent (Ulmer and Trommsdorff, 1995; Wunder and Schreyer, 1997).

Thermodynamic work on the serpentinite multisystem predicts the crystallization of antigorite (Atg) at the expense of chrysotile (Chr) or lizardite (Lz), according to the following reactions (Evans, 2004) with forsterite (Fo) and brucite (Brc):

$$17\mathrm{Lz/Chr} = \mathrm{Atg} + 3\mathrm{Brc} \quad (1)$$

$$20\mathrm{Chr/Lz} = \mathrm{Atg} + 6\mathrm{Fo} + 9\mathrm{H_2O} \quad (2)$$

$$16\mathrm{Lz/Chr} + 2\mathrm{SiO_2,aq} = \mathrm{Atg} + \mathrm{H_2O} \quad (3)$$

Reactions (1) and (2) are thermodynamically favorable for temperatures above 300 °C and 380 °C respectively (Evans, 2004), while at lower temperatures, the conversion of lizardite to antigorite is thermodynamically more efficient with a modest introduction in the serpentinite multisystem of SiO_2 (e.g., Evans, 2004). Thus, Reaction (2) cannot explain the crystallization of antigorite at low temperatures (<380 °C according to Evans (2004)). In contrast, we clearly observe the direct crystallization of veins of antigorite at the expense of lizardite starting at 320 °C in the presence of metasediments. Moreover, we observe a general enrichment in SiO_2 throughout the antigorite (Fig. 6) that is correlated with a whole-rock SiO_2 enrichment along the metamorphic gradient (Lafay et al., in press). This finding suggests the onset of antigorite crystallization at 320 °C, assisted by SiO_2-rich fluids, according to Reaction (3), by dissolution–precipitation processes (Fig. 8). Rüpke et al. (2004) have shown that above a depth of 50 km (T<300 °C), oceanic sediments release almost 50% of their initial water content. This fluid is enriched in volatile elements and silica and potentially hydrated the mantle wedge (e.g., Bebout and Barton, 1989; Bebout et al., 1999). Fluid exchange between the subducted oceanic sediments and our serpentinite samples is clearly demonstrated by the enrichment of volatile elements, particularly in the antigorite (Lafay et al., in press). Thus, the most favorable circumstances for silicification are waters that are equilibrated with sedimentary rocks in the Alpine wedge and that percolated into the serpentinites, as observed in the Catalina Schist in California (Bebout and Barton, 1989; Bebout et al., 1999). As already discussed, we also observed the transformation of lizardite into antigorite, suggesting the progression of Reaction (1) between 340 and 380 °C. In the natural samples presented here, this reaction occurred at slightly higher temperatures than were predicted by thermodynamic calculations (260–310 °C at 10 kbar, Evans, 2004).

Brucite has not been detected as an antigorite byproduct in the undeformed sample (Vi01), which is supported by the absence of characteristic XRD peaks in the studied samples. However, brucite is locally observed in the Monviso sheared serpentinites (Fig. 5d′). In the undeformed sample, the absence of brucite could be interpreted either as the result of a lower olivine hydration with respect to enstatite hydration (precluding the release of Mg necessary to the brucite crystallization) or as the consumption of brucite during prograde reactions. In contrast, in the sheared sample (Vi02), metamorphic olivine crystallized at the expense of antigorite and brucite according to the Reaction (4) in Fig. 8:

$$\mathrm{Atg} + \mathrm{Brc} = 2\mathrm{Fo} + 3\mathrm{H_2O} \quad (4)$$

This reaction suggests the onset of antigorite destabilization, compatible with a decrease of the whole-rock L.O.I from 13 wt.% to<12 wt.% (Lafay et al., in press). In the natural studied samples, this reaction occurred at T≥460 °C and P>12 kbar, as predicted by thermodynamic calculations (Evans, 2004).

8. Conclusion

Raman spectroscopy and XRD are efficient methods for identifying different species of serpentine because serpentine optical identification is difficult. In addition, various serpentine species are often interpenetrated, and Raman micro-spectrometry proves to be a useful micro-characterization tool for resolving structural differences at the scale of the various grain generations. The application of these

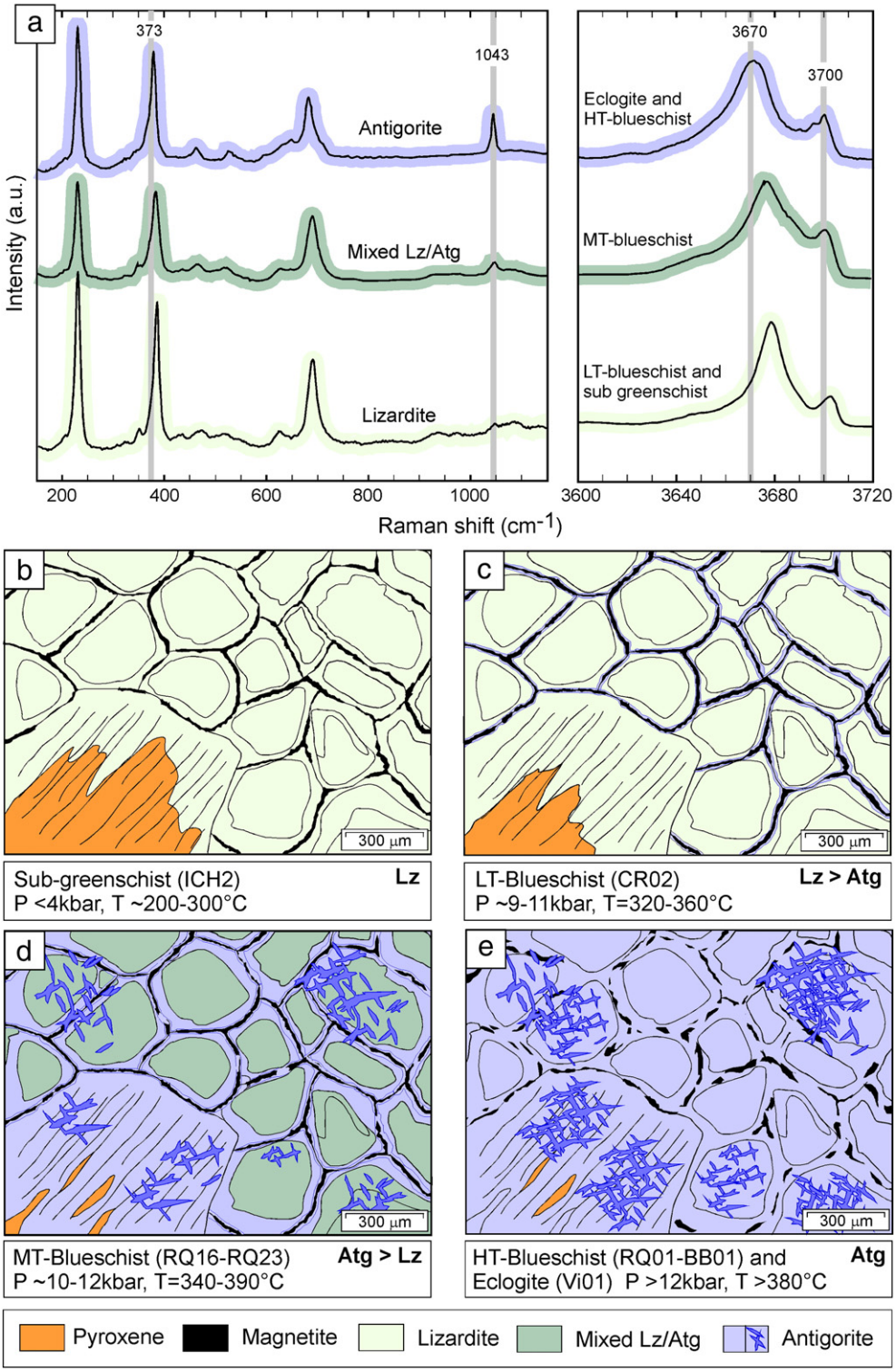

Fig. 7. Idealized sketch determined from natural serpentinites that shows the evolution of the antigoritization processes under a HP metamorphic gradient. (a) Characteristic Raman spectra of serpentine species from the study area. The bands of antigorite (373, 1043, 3670 and 3700 cm^{-1}) are indicated in grey. (b) In sub-greenschist conditions, only lizardite is present. (c) In LT-blueschist, antigorite appears along the lizardite grain boundaries via a dissolution–precipitation process. (d) In MT-blueschist, the antigorite becomes the major phase. The veins of antigorite at the lizardite grain boundaries widen and the cores of lizardite show a mixed lizardite/antigorite Raman spectra. (e) In HT-blueschist, antigorite becomes the sole serpentine variety. Antigorite develops infra-millimetric blades superimposed over the original mesh texture.

methods to samples from the Alps shows that lizardite is preserved under sub-greenschist facies conditions in the oceanic environment and ophiolites. Antigorite progressively replaces lizardite under LT- to MT-blueschist facies conditions (320–390 °C) and is the sole serpentine phase under HT-blueschist to eclogites facies conditions (>380 °C). Our study shows several generations of serpentine in sea-floor and metamorphic processes. Below 320 °C, lizardite and chrysotile are the only stable serpentine species. Between 320 °C and 390 °C, lizardite and antigorite coexist and antigorite develops at the expense of lizardite through two processes. Antigorite first

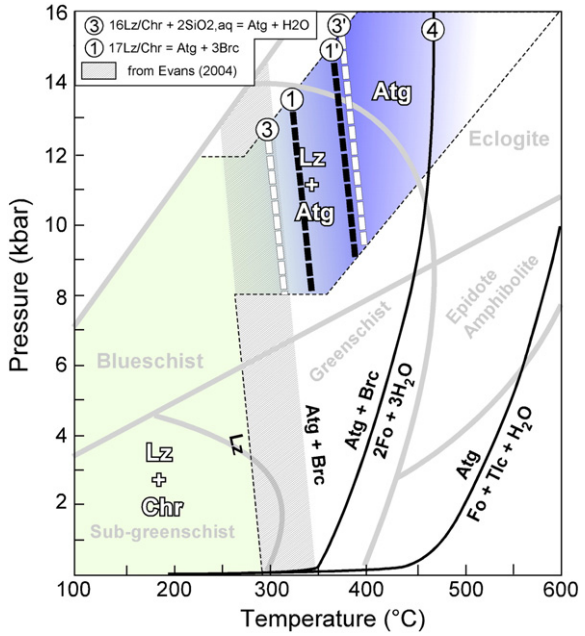

Fig. 8. Phase diagram of antigorite and lizardite (after Evans, 2004): Lz, lizardite; Atg, antigorite; Chr, chrysotile; Fo, forsterite; Tlc, talc; Brc, brucite. Reactions (1) and (3) correspond to the onset of the reactions while (1′) and (3′) correspond to the end of these reactions with the complete consumption of lizardite. Metamorphic facies are from Spear (1993). The natural stability field domain of coexisting lizardite and antigorite is restricted to a temperature range between ~320 and 390 °C. At 390 °C and above, the lizardite is entirely replaced by antigorite. Above 460 °C, Reaction (4) results in the onset of crystallization of olivine. Between 320 and 390 °C, the antigorite develops though Reaction (3) in the presence of SiO_2-rich fluids by dissolution–precipitation processes. Between 340 and 380 °C, Reaction (2) is also observed in the core of lizardite antigorite by dissolution precipitation process.

appears at the lizardite grain boundaries through dissolution–precipitation processes in the presence of SiO_2. We propose that this fluid comes from the local dehydration of the surrounding metasediments in subduction environments. Antigorite also crystallizes in the cores of the lizardite mesh through dissolution–precipitation process at slightly higher temperatures, between 340 °C and 380 °C. This transition is characterized by mixed lizardite/antigorite Raman spectra. Above 390 °C and 12 kbar, lizardite is absent and antigorite is the only stable serpentine species. Above 460 °C, antigorite begins to destabilize into olivine. In sheared sample, olivine crystallizes at the expense of antigorite and brucite while in the undeformed sample brucite is not detected, although this mineral is theoretically involved in the transition from lizardite to antigorite. We propose that the brucite produced at low temperatures is mostly consumed at higher temperatures and remains a transitional phase. This process would explain why brucite is rarely observed in natural samples in oceanic and subduction environments worldwide.

Acknowledgments

This study was supported by the *Agence Nationale de la Recherche* project no. ANR-08-BLAN-0303-01 “Erosion and Relief Development in the Western Alps”, the SUBDEF grant no. ANR-08-BLAN-0192 and the Labex OSUG2020. N. Findling is thanked for the XRD analyses (University of Grenoble 1). We gratefully acknowledge constructive reviews by BW. Evans, M. Scambelluri and an anonymous reviewer.

References

Agard, P., Vidal, P., Goffé, B., 2001. Interlayer and Si content of phengite in HP-LT carpholite-bearing metapelites. Journal of Metamorphic Geology 19, 479–495.

Agard, P., Monié, P., Jolivet, L., Goffé, B., 2002. Exhumation of the Schistes Lustrés complex: In situ laser probe Ar-40/Ar-39 constraints and implications for the western Alps. Journal of Metamorphic Geology 20, 599–618.

Alt, J.C., Shanks, W.C., 2003. Serpentinization of abyssal peridotites from the MARK area, Mid-Atlantic ridge, sulphur geochemistry and reaction modelling. Geochimica et Cosmochimica Acta 67, 641–653.

Andréani, M., Mével, C., Boullier, A.M., Escartin, J., 2007. Dynamic control on serpentine crystallisation in veins: constraints on hydration processes in oceanic peridotites. Geochemistry, Geophysics, Geosystems Q02012. http://dx.doi.org/10.1029/2006GC001373.

Angiboust, S., Langdon, R., Agard, P., Waters, D., Chopin, C., 2012. Eclogitization of the Monviso ophiolite (W. Alps) and implications on subduction dynamics. Journal of Metamorphic Geology 30, 37–61.

Auzende, A.L., Devouard, B., Guillot, S., Daniel, I., Baronnet, A., Lardeaux, J.M., 2002. Serpentinites from Central Cuba: petrology, and HRTEM study. European Journal of Mineralogy 14, 905–914.

Auzende, A.L., Daniel, I., Reynard, B., Lemaire, C., Guyot, F., 2004. High-pressure behaviour of serpentine minerals: a Raman spectroscopic study. Physics and Chemistry of Minerals 31 (5), 269–277.

Auzende, A.L., Guillot, S., Devouard, B., Baronnet, A., 2006. Serpentinites in Alpine convergent setting: effects of metamorphic grade and deformation on microstructures. European Journal of Mineralogy 18, 21–33.

Bard, D., Yarwood, J., Tylee, B., 1997. Asbestos fibre identification by Raman microspectroscopy. Journal of Raman Spectroscopy 28, 803–809.

Baronnet, A., Belluso, E., 2002. Microstructures of the silicates: key information about mineral reactions and a link with the Earth and materials sciences. Mineralogical Magazine 66, 709–732.

Bebout, G.E., Barton, M.K., 1989. Fluid flow and metasomatism in a subduction zone hydrothermal system: Catalina Schist terrane, California. Geology 17, 976–980.

Bebout, G.E., Ryan, J.G., Leeman, W.P., Bebout, A.E., 1999. Fractionation of trace elements by subduction-zone metamorphism, effect of convergent-margin thermal evolution. Earth and Planetary Science Letters 171, 63–81.

Beyssac, O., Goffé, B., Chopin, C., Rouzaud, N., 2002. Raman spectra of carbonaceous material in metasediments: a new geothermometer. Journal of Metamorphic Geology 20, 859–871.

Beyssac, O., Goffé, B., Petitet, J.P., Froigneux, E., Moreau, M., Rouzaud, J.N., 2003. On the characterisation of disordered and heterogeneous carbonaceous materials by Raman spectrometry. Spectrochimica Acta 59, 2267–2276.

Beyssac, O., Simoes, M., Avouac, J.P., Farley, K.A., Chen, Y.G., Goffé, B., Beyssac, O., Simoes, M., Avouac, J.P., Farley, K.A., Chen, Y.G., Goffé, B., 2007. Late Cenozoic metamorphic evolution and exhumation of Taiwan. Tectonics 26, 32 (TC6001).

Boudier, F., Baronnet, A., Mainprice, D., 2010. Serpentine mineral replacements of natural olivine and their seismic implications: oceanic lizardite versus subduction-related antigorite. Journal of Petrology 51, 495–512.

Bromiley, G.D., Pawley, A.R., 2003. The stability of antigorite in the systems MgO–SiO_2–H_2O (MSH) and MgO–Al_2O_3–SiO_2–H_2O (MASH): the effects of Al^{3+} substitution on high-pressure stability. American Mineralogist 88, 99–108.

Debret, B., Nicollet, C., Andréani, M., Schwartz, S., Godard, M., 2013. Three steps of serpentinization in an eclogized oceanic serpentinization front (Lanzo massif — Western Alps). Journal of Metamorphic Geology. http://dx.doi.org/10.1111/jmg.12008.

Deer, W.A., Howie, R.A., Zussman, J., 1992. An Introduction to the Rock-Forming Minerals, 2nd edition. Longman Scientific & Technical, Harlow.

Deville, E., Fudral, S., Lagabrielle, Y., Marthaler, M., Sartori, M., 1992. From oceanic closure to continental collision: a synthesis of the Schistes lustrés metamorphic complex of the western Alps. Geological Society of America Bulletin 104, 127–139.

Dumont, T., Schwartz, S., Guillot, S., Simon-Labric, T., Tricart, P., Jourdan, S., 2012. Structural and sedimentary records of the Oligocene revolution in the Western Alps. Journal of Geodynamics 56–57, 18–38.

Evans, B.W., 2004. The serpentinite multisystem revisited: chrysotile is metastable. International Geology Review 46, 479–506.

Evans, B.W., Tromsdorff, V., 1978. Petrogenesis of garnet lherzolite, Cima di Gagnone, Lepontine Alps. Earth and Planetary Science Letters 39, 55–71.

Frost, B.R., Beard, J.S., 2007. On silica activity and serpentinization. Journal of Petrology 49, 1351–1368.

Ganne, J., Bertrand, J.M., Fudral, S., 2005. Fold interference pattern at the top of basement domes and apparent vertical extrusion of HP rocks (Ambin and South Vanoise massifs, western Alps). Journal of Structural Geology 27, 553–570.

Goffé, B., Schwartz, S., Lardeaux, J.M., Bousquet, R., 2004. Metamorphic structures of the Western and Ligurian Alps. Mitteilungen der Österreichischen Mineralogischen Gessellschaft 149, 125–144.

Groppo, C., Compagnoni, R., 2007. Metamorphic veins from the serpentinites of the Piemonte Zone, western Alps, Italy: a review. Periodico di Mineralogia 76, 127–153.

Groppo, C., Rinaudo, C., Cairo, S., Gastaldi, D., Compagnoni, R., 2006. Micro-Raman spectroscopy for quick and reliable identification of serpentinite minerals from ultramafics. European Journal of Mineralogy 18, 319–329.

Guillot, S., Hattori, K., Agard, P., Schwartz, S., Vidal, O., 2009. Exhumation processes in oceanic and continental subduction contexts: a review. In: Lallemand, S., Funiciello, F. (Eds.), Subduction Zone Dynamics. Springer, Verlag Berlin Heidelberg, pp. 175–204. http://dx.doi.org/10.1007/978-3-540-87974-9.

Hattori, K., Guillot, S., 2007. Geochemical character of serpentinite associated with high to ultrahigh pressure rocks in Alps, Cuba and the Himalayas: recycling of elements in subduction zones. Geochemistry, Geophysics, Geosystems Q09010. http://dx.doi.org/10.1029/2007GC001594.

Kloprogge, J.T., Frost, R.L., Rintoul, L., 1999. Single crystal Raman microscopic study of the asbestos mineral chrysotile. Journal of Physical Chemistry 1, 2559–2564.

Lafay, R., Montes-Hernandez, G., Janots, E., Chiriac, R., Findling, N., Toche, F., 2012. Mineral replacement rate in olivine by chrysotile and brucite under high alkaline conditions. Journal of Crystal Growth 347, 62–72.

Lafay R., Deschamps F., Schwartz S., Guillot S., Godard M., Nicollet C., in press.High-pressure serpentinites, a trap-and-release system controlled by metamorphic conditions: Example from the Piedmont zone of the western Alps. Chem. Geol.

Lagabrielle, Y., Polino, R., 1988. Un schéma structural du domaine des Schistes lustrés ophiolitifère au nord-ouest du massif du Mont Viso (Alpes Sud-Occidentales) et ses implications. Comptes Rendus de l'Académie des Sciences 306, 921–928.

Lanari, P., Guillot, S., Schwartz, S., Vidal, O., Tricart, P., Riel, N., Beyssac, O., 2012. Diachronous evolution of the alpine continental wedge: evidences from P–T estimates in the Briançonnais Zone houillère (France-Western Alps). Journal of Geodynamics 56–57, 39–54.

Lardeaux, J.M., Schwartz, S., Paul, A., Tricart, P., Guillot, S., Béthoux, N., Masson, F., 2006. A crustal-scale cross section of the southwestern Alps combining geophysical and geological imagery. Terra Nova 18, 412–422.

Lemoine, M., Tricart, P., Boillot, G., 1987. Ultramafic and gabbroic ocean floor of the Ligurian Tethys (Alps, Corsica, Apennines): in search of a genetic model. Geology 15, 622–625.

Lewis, I., Chaffin, N., Gunter, M., Griffiths, P., 1996. Vibration spectroscopic studies of asbestos and comparison of suitability for remote analysis. Spectrochimica Acta Part A 52, 315–328.

Li, X.P., Rahn, M., Bucher, K., 2004. Serpentinites of the Zermatt–Saas ophiolite complex and their texture evolution. Journal of Metamorphic Geology 22, 159–177.

Mellini, M., Ferraris, G., Compagnoni, R., 1985. Carlosturanite: HRTEM evidence of a polysomatic series including serpentine. American Mineralogist 70, 773–781.

Mellini, M., Trommsdorff, V., Compagnoni, R., 1987. Antigorite polysomatism: behaviour during progressive metamorphism. Contributions to Mineralogy and Petrology 97, 147–155.

Mével, C., Caby, R., Kienast, J.R., 1978. Amphibolite facies conditions in oceanic crust: example of amphibolitized flaser gabbros and amphibolites from the Chenaillet ophiolite massif (Hautes Alpes, France). Earth and Planetary Science Letters 39, 98–108.

Miyashiro, A., Shido, F., Ewing, M., 1969. Composition and origin of serpentinites from the Mid-Atlantic Ridge near 24 and 30°N. Contributions to Mineralogy and Petrology 23, 117–127.

O'Hanley, D.S., 1996. Serpentinites. Oxford Monographs on Geology and Geophysics 34 277 pp.

Padron-Navarta, J.A., Sanchez-Vizcaino, V.L., Garrido, C.J., Gómez-Pugnaire, M.T., Jabaloy, A., Capitani, G.C., Mellini, M., 2008. Highly ordered antigorite from Cerro del Almirez HP-HT serpentinites, SE Spain. Contributions to Mineralogy and Petrology 156, 679–688.

Padron-Navarta, J.A., Hermann, J., Garrido, C.J., Sanchez-Vizcaino, V.L., Gómez-Pugnaire, M.T., 2010. An experimental investigation of antigorite dehydration in natural silica-enriched serpentinite. Contributions to Mineralogy and Petrology 159, 25–42.

Putnis, A., 2009. Mineral replacement reactions. Reviews in Mineralogy and Geochemistry 70, 87–124.

Quirico, E., Montagnac, G., Rouzaud, J.N., Bonal, L., Bourot-Denise, M., Dufer, S., Reynard, B., 2009. Precursor and metamorphic condition effects on Raman spectra of poorly ordered carbonaceous matter in chondrites and coals. Earth and Planetary Science Letters 287, 185–193.

Reynard, B., Wunder, B., 2006. High-pressure behavior of synthetic antigorite in the $MgO–SiO_2–H_2O$ system from Raman spectroscopy. American Mineralogist 91, 459–462.

Rinaudo, C., Gastaldi, D., Belluso, E., 2003. Characterization of chrysotile, antigorite, and lizardite by FT-Raman spectroscopy. Canadian Journal of Mineralogy 41, 883–890.

Rosenbaum, G., Lister, G.S., 2005. The Western Alps from the Jurassic to Oligocene: spatio-temporal constraints and evolutionary reconstructions. Earth-Science Reviews 69, 281–306.

Rüpke, L.H., Morgan, J.P., Hort, M., Connolly, J.A., 2004. Serpentine and the subduction water cycle. Earth and Planetary Science Letters 223, 17–34.

Scambelluri, M., Müntener, O., Hermann, J., Piccardo, G.B., Trommsdorff, V., 1995. Subduction of water into the mantle-history of an alpine peridotite. Geology 23, 459–462.

Schwartz, S., Lardeaux, J.M., Guillot, S., Tricart, P., 2000. The diversity of eclogitic metamorphism in the Monviso ophiolitic complex, western Alps, Italy. Geodinamica Acta 13, 169–188.

Schwartz, S., Allemand, P., Guillot, S., 2001. Numerical model of the effect of serpentinites on the exhumation of eclogitic rocks: insights from the Monviso ophiolitic massif (Western Alps). Tectonophysics 42, 193–206.

Schwartz, S., Lardeaux, J.M., Tricart, P., Guillot, S., Labrin, E., 2007. Diachronous exhumation of subducted HP metamorphic rocks from southwestern Alps: evidences from fission-track analysis. Terra Nova 19, 133–140.

Schwartz, S., Tricart, P., Lardeaux, J.M., Guillot, S., Vidal, O., 2009. Final exhumation of an accretionary wedge (Queyras Schistes Lustrés, Western Alps): deformation sequence and associated P–T-t path. Geological Society of America Bulletin 121, 502–518.

Spear, F.S., 1993. Metamorphic phase equilibria and pressure–temperature–time paths. Mineralogical Society of America, Washington, D.C. (799 pp.).

Tricart, P., 1984. From passive margin to continental collision: a tectonic scenario for the western Alps. American Journal of Science 284, 97–120.

Tricart, P., Lemoine, M., 1986. From faulted blocks to megamullions and megaboudins-Tethyan heritage in the structure of the western Alps. Tectonics 5, 95–118.

Tricart, P., Schwartz, S., 2006. A north–south section across the Queyras Schistes lustrés (Piedmont zone, Western Alps): syncollision refolding of a subduction wedge. Eclogae Geologicae Helvetiae 99, 429–442.

Trommsdorff, V., Sanchez-Vizcaino, V.L., Gomez-Pugnaire, M.T., Muntener, O., 1998. High pressure breakdown of antigorite to spinifex-textured olivine and orthopyroxene, SE Spain. Contributions to Mineralogy and Petrology 132, 139–148.

Ulmer, P., Trommsdorff, V., 1995. Serpentinite stability to mantle depths and subduction related magmatism. Science 268, 858–861.

Viti, C., Mellini, M., 1996. Vein antigorites from Elba Island, Italy. European Journal of Mineralogy 8, 423–432.

Wicks, F.J., O'Hanley, D.S., 1988. Serpentine minerals: structures and petrology. Rev Mineral, 19. In: Bailey, S.W. (Ed.), Hydrous Phyllosilicates, pp. 91–167.

Wunder, B., Schreyer, W., 1997. Antigorite: high pressure stability in the system $MgO–SiO_2–H_2O$ (MSH). Lithos 41, 213–227.